# Gigahertz Low-Loss and Wideband S0 Mode Lithium Niobate Acoustic Delay Lines

Ruochen Lu, *Student Member, IEEE*, Tomás Manzaneque, *Member, IEEE*, Yansong Yang, *Student Member, IEEE*, Ming-Huang Li, *Member, IEEE*, and Songbin Gong, *Senior Member, IEEE*

***Abstract*— We present the first group of gigahertz S0 mode low loss and wideband acoustic delay lines (ADLs). The ADLs use a single-phase unidirectional transducers (SPUDT) design to launch and propagate the S0 mode in an X-cut lithium niobate thin film with large electromechanical coupling and low damping. In this work, the theoretical performance bounds of S0 mode ADLs are first investigated, significantly surpassing those in state-of-the-art. The design tradeoffs of S0 mode ADLs, when scaled to the gigahertz frequency range, are also discussed. The fabricated miniature ADLs show a fractional bandwidth (FBW) of 4% and a minimum insertion loss (IL) of 3.2 dB, outperforming the incumbent surface acoustic wave (SAW) counterparts, and covering a wide range of delays from 20 to 900 ns for digitally addressable delay synthesis. Multiple ADLs with center frequencies from 0.9 to 2 GHz have been demonstrated, underscoring their great frequency scalability. The propagation properties of S0 waves in lithium niobate at the gigahertz range are experimentally extracted. The demonstrated ADLs can potentially enable wide-range and high-resolution delay synthesis that is highly sought after for the self-interference cancellation in full-duplex radios.**

***Index Terms*— Acoustic delay lines (ADLs), full-duplex, lithium niobate, microelectromechanical systems, piezoelectricity, S0 modes, self-interference cancellation (SIC).**

## I. Introduction

FULL-DUPLEX radios, where the transmitters and receivers operate simultaneously in the same frequency band, have sparked great research interest due to their great potential to enhance spectrum utilization efficiency and reduce networking complexity [1]–[3]. Among the outstanding challenges for full-duplex radios, self-interference (SI) presents the most formidable contest to implementing full-duplex radios [4], [5]. Due to the absence of frequency or time-domain multiplexing, SI happens when the high-power transmitted signals are reflected from antenna packaging or obstacles in the ambiance, and inadvertently received by the highly sensitive receiver, typically after 0.01–1-$\mu$s delay [6], [7]. To reduce the SI, i.e., attain SI cancellation (SIC), one approach is to provide wideband time-domain equalization using true time delays [2], [8]. In such a method, a fraction of the transmitted signal is sent into the time-domain equalizer that emulates the channel transfer function of the SI before it is combined with the SI to render cancellation through destructive interference. To accommodate the dynamic in-field conditions, such a system is typically required to provide reconfigurable delays and tunable attenuations (Fig. 1). The challenge with such a method is that, although chip-scale tunable attenuation is readily attainable [9], miniature delay synthesis over a sufficiently wide bandwidth (BW) and a necessary delay range remains inaccessible. The unavailability of wide-range delay synthesis originates from the fact that the electromagnetic (EM) delay lines in the existing prototypes [10] can hardly provide delays more than 1 ns on chip scale due to the fast group velocities of EM waves in state-of-the-art slow wave waveguiding structures. Therefore, EM-based delay synthesis is inadequate for enabling full-duplex in urban environments with dense reflectors (e.g., moving vehicles and buildings) [6]. Moreover, the dynamic range of EM-based SIC is also limited. The minimum insertion loss (IL) in the cancellation path is required to be no larger than that in the free space. However, the intrinsically high propagation loss (PL) in the EM delay lines leads to high IL. Moreover, the additional IL from the directional coupler strengthens the requirement of IL, which is challenging for the EM delay lines. Therefore, acoustic delay lines (ADLs) with remarkably smaller sizes and lower PL [11] are an excellent alternative platform for a compact, wideband, and low-loss delay synthesis that is also capable of being scaled toward the gigahertz frequency range and overcoming the shortcomings of the EM structures.

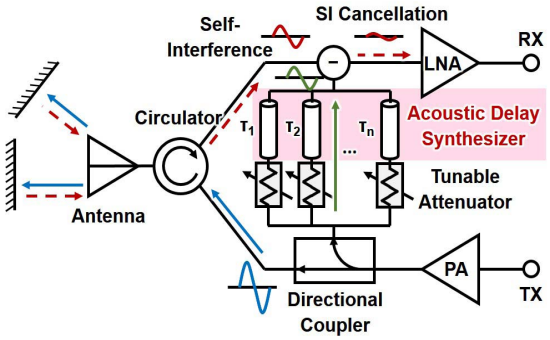


Fig. 1. SIC in a full-duplex transceiver with an acoustic delay synthesizer.

Manuscript received January 8, 2019; accepted May 3, 2019. Date of publication May 10, 2019; date of current version August 1, 2019. This work was supported by the Defense Advanced Research Projects Agency Microsystems Technology Office under Program "Near Zero Power RF and Sensor Operations." *(Corresponding author: Ruochen Lu.)*

The authors are with the Department of Electrical and Computing Engineering, University of Illinois at Urbana–Champaign, Urbana, IL 61801 USA (e-mail: rlu10@illinois.edu; tmanzane@illinois.edu; yyang165@illinois.edu; mhli@illinois.edu; songbin@illinois.edu).

Digital Object Identifier 10.1109/TUFFC.2019.2916259

In an ADL, the radio frequency (RF) signals are first converted into the acoustic domain by the transducers on one end of the ADL via piezoelectricity [12]. The signals then propagate as acoustic waves and experience the designed delay before they are turned back into the electrical signals by the transducers on the other end. In the past, RF ADLs were mainly realized using surface acoustic waves (SAW) technologies [13], [14] due to their compact sizes and easy fabrication processes [15]. ADLs were used to enable time delays [12], filtering [16], and correlation [11] for improving the signal-to-noise ratios in radar front ends. It can also be used for various sensing applications [17], [18] and the construction of nonreciprocal networks [19], [20]. However, it was difficult for these SAW demonstrations to provide sufficiently low IL and wide BW simultaneously for the SIC applications even when custom designed unidirectional transducers were adopted [21], [22]. Such a performance limit arises from the intrinsic tradeoff between the IL and fractional BW (FBW), which are fundamentally imposed by the attainable reflectivity of the distributed reflectors and the maximum electromechanical coupling ($k^2$) of the SAW modes [23]. In addition, the transducer-induced SAW scattering into the substrate further exacerbates the PL of the SAW and the tradeoff between IL and delay. Therefore, to work toward an acoustic delay synthesizer, the fundamental performance bounds must be considerably lifted by resorting to a new piezoelectric platform with higher coupling, larger available reflectivity, and better-confined waveguiding at the same time.

Recently, laterally vibrating modes in thin-film lithium niobate ($LiNbO_3$), namely, the fundamental shear horizontal (SH0) mode [24]–[27] and fundamental symmetrical (S0) mode [28]–[30], have been recently explored in ADL structures [1], [31]–[34] for their simultaneously large $k^2$ and low loss [35]–[37]. Compared to the previously published thin-film delay structures based on laterally vibrating modes in thin-film structures [38]–[40], the large coupling can be harnessed to widen the BW of ADLs, while the confined waveguiding in a suspended $LiNbO_3$ thin film can lower PL and thus IL. Moreover, reflectors on a suspended thin film can provide more substantial reflections in comparison to the same type of reflectors on an SAW structure, thereby further improving the tradeoff between IL and BW. Despite the demonstrated record-breaking performance of $LiNbO_3$ ADLs using lateral modes, these previous reports focus on devices with operating frequencies below 300 MHz and not suitable for the commercial wireless communication bands at 700 MHz or beyond. To advance $LiNbO_3$ ADLs for full-duplex applications in commercial bands, this work aims to demonstrate the first gigahertz range, low-loss, wideband ADLs based on the S0 mode in $LiNbO_3$.

In this study, the design space of gigahertz S0-mode ADLs is first discussed. The fabricated miniature ADLs show an FBW of 4% and a minimum IL of 3.2 dB at a center frequency of 0.96 GHz. Various delays ranging from 20 to 900 ns have been obtained for a future demonstration of digitally addressable delay synthesis. Multiple ADLs with center frequencies from 0.9 to 2 GHz have been demonstrated. The PL of the S0 mode at the gigahertz frequency range is also experimentally measured for the first time, showing a PL of 6.08 dB/$\mu$s at 0.96 GHz or 0.0055 dB/$\lambda$ (dB per wavelength). The demonstrated ADLs can potentially provide wide-range and high-resolution reconfigurable delays that are highly sought after for the SIC in full-duplex radios.

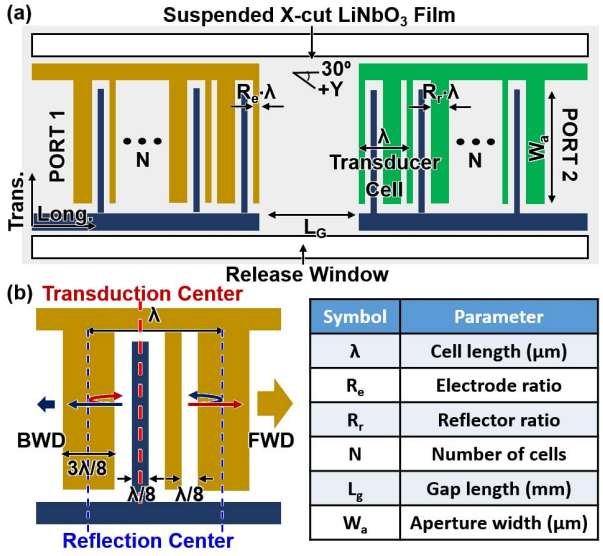


Fig. 2. (a) Mock-up of an S0 mode ADL with a pair of SPUDT transducers on a suspended X-cut $LiNbO_3$ thin film. The transverse and longitudinal directions are labeled. (b) Layout of an SPUDT unit cell.

This paper is organized as follows. Section II provides a general discussion on the design of the S0 mode ADLs. The ADL topology is first introduced, followed with a theoretical demonstration on how S0 mode ADLs break the fundamental performance limits of the incumbent SAW technologies. The design is then supported by the finite-element analysis (FEA), specifically focusing on gigahertz ADL design and the acoustic wave propagation characteristics in the thin-film waveguiding structures. Section III summarizes the fabrication process and presents the fabricated gigahertz ADLs. Section IV offers the measurement results and discussions of the devices with different gap lengths and different center frequencies. The S0 wave propagation characteristics, including PL and phase velocities, are experimentally derived. Finally, the conclusion is stated in Section V.

## II. S0 Mode Acoustic Delay Line Design

### A. Unidirectional Acoustic Delay Line Overview

The schematic of a typical S0 mode ADL is shown in Fig. 2 with the key parameters explained in the inset table. The ADL consists of 135-nm aluminum interdigitated transducers on top of a suspended 800-nm $LiNbO_3$ thin film. The device is oriented at 30° to the $+y$-axis in X-cut $LiNbO_3$ for harnessing the high phase velocity and large coupling of the S0 mode. S0 is chosen to build gigahertz ADLs for two primary reasons. First, high $k^2$ up to 40% is accessible in X-cut $LiNbO_3$, thus allowing a better BW-IL tradeoff for ADLs [41]–[43]. Second, in contrast to SH0, the high phase velocity (over 7000m/s) of S0 permits the scaling to higher frequencies with larger feature sizes [44].

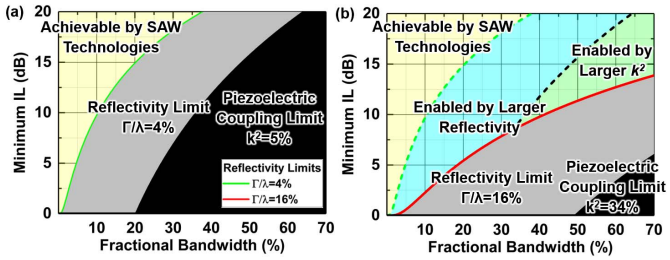


Fig. 3. Tradeoff between the minimum IL and FBW for SPUDT ADLs in (a) conventional SAW and (b) S0-mode $LiNbO_3$ platform, showing piezoelectric (black) and reflectivity limits (gray).

The transducers on the opposite ends of the ADL adopt the design of single-phase unidirectional transducers (SPUDT) [16], [22], [23]. As shown in Fig. 2(b), the SPUDTs are composed of cascaded transducer unit cells that each include a pair of transduction electrodes ($\lambda/8$ wide) and one distributed acoustic reflector ($3\lambda/8$ wide) shorted to the ground [22], [23]. In each cell, the two reflectors are arranged on the opposite sides of the transduction center nonsymmetrically with different spacings of $3\lambda/8$ and $5\lambda/8$. As shown in Fig. 2(b), the transduction center referred herein is defined as the center of the blue electrode. After launching from the transduction center, the acoustic wave propagating toward the left gets partially reflected from the left-side reflector and starts traversing in the forward direction (FWD, i.e., right in Fig. 2). As the reflected acoustic wave returns to the transduction center, it experiences a total of $-2\pi$ phase delay that results from $-1.5\pi$ phase delay from the propagation and a $-0.5\pi$ phase delay from the reflection, thereby the reflected wave constructively interferes with the wave directly launched toward the FWD. On the other hand, the wave propagating toward the FWD experiences $-2.5\pi$ phase delay from the propagation and a $-0.5\pi$ phase delay from the reflection. The signal sees a total delay of $-3\pi$ upon its arrival back to the transducer center and destructively interferes with the wave directly launched toward the backward direction (BWD). With a sufficient amount of cascading reflections distributed in the unit cells, near perfect cancellation of the BWD wave propagation can be achieved, resulting in the removal of the bidirectionality in the transducers and a 6-dB reduction in the IL of the ADL.

### *B. Performance Limits of Acoustic Delay Lines*

The performance of S0 ADLs can be then compared with the incumbent SAW technology regarding their fundamental limits. As mentioned earlier, two factors, namely, $k^2$ and the reflectivity in SPUDTs, fundamentally limit the performance of SPUDT-based ADLs. Their impact on delay line performance has been studied in [23] and readopted as shown in Fig. 3(a) for SAW devices. $k^2$ is intrinsically bounded by the piezoelectric properties of the material and effective coupling efficiency of the transducer for a given mode. It sets the limit on the maximum FBW over which the impedance matching can be attained without imposing a significant IL. For devices working beyond the maximum FBW, the IL can be expressed as [23], [45]

$$\mathrm{IL} = \mathrm{FBW}^2 \cdot Q_T / c_{\mathrm{piezo}}, \quad \text{when FBW} > \sqrt{c_{\mathrm{piezo}}/Q_T} \tag{1}$$

$$c_{\mathrm{piezo}} = \frac{v_f - v_m}{v_f} \cdot \left[1 + \frac{3(v_f - v_m)}{2v_f}\right] \tag{2}$$

where $Q_T$ is the normalized quality factor of the transducer and is only determined by the transduction structure. $c_{\mathrm{piezo}}$ is the material piezoelectric constant determined by the material coupling coefficient and can be calculated through the phase velocities of the acoustic wave in the thin film sections with free surface $v_f$ and metalized surface $v_m$. For our design with $Q_T$ of 0.6594 [23], $v_f$ of 7018 m/s, and $v_m$ of 6047 m/s [44], the maximum coupling coefficient is 35%. Based on (1), $k^2$ of 35% translates to a maximum FBW of 50%, beyond which a larger FBW has to come at the cost of a higher IL. In other words, the black region shown in Fig. 3(b) is forbidden and cannot be accessed.

On the other hand, the attainable reflections in the embedded reflectors limit the unidirectionality of the transducer pairs and thereby the IL of the ADL. The dependence of IL on reflectivity can be expressed as [23]

$$\mathrm{IL} = 1 - e^{-\Gamma_\lambda/\mathrm{FBW}} \tag{3}$$

where $\Gamma_\lambda$ is the reflection per wavelength. Equation (3) quantitatively explains that a platform with a lower $\Gamma_\lambda$ requires more cells/reflectors to achieve the same unidirectionality and IL and intrinsically leads to a smaller FBW due to the dependence of transducer frequency-domain response on the number of cells ($\mathrm{FBW}_{\mathrm{transducer}} \sim 1/N$). $\Gamma_\lambda$ can be calculated based on a previously developed model that separates the reflection into the mechanically and electrically induced reflections [31]. The mechanical reflection is caused by different effective acoustic impedances in the sections of $LiNbO_3$ with and without electrodes, while the electrical reflection is induced by the constant potential boundary condition in the metalized $LiNbO_3$ sections. The mechanical reflection per unit cell can be calculated as [31]

$$\Gamma_m = \Gamma_{\mathrm{su}} \mathrm{e}^{j\alpha} \frac{1 - e^{-j2\alpha}\left(1 - \Gamma_{\mathrm{su}}^2\right)}{1 - \Gamma_{\mathrm{su}}^2 e^{-j2\alpha}} \tag{4}$$

where $\Gamma_m$ is the mechanical reflection coefficient at the reflection center, $\Gamma_{\mathrm{su}}$ is the step-up reflection coefficient, and $\alpha$ is the electrical width of the reflector, which is $3\pi/4$ for our SPUDT design. $\Gamma_{\mathrm{su}}$ is obtained from COMSOL frequency-domain FEA. In the FEA, the mechanical reflection coefficient of a single reflector is obtained. $\Gamma_{\mathrm{su}}$ is then extracted through the multireflection theory. A detailed explanation can be found in [31]. For a stack of 135-nm aluminum on 800-nm $LiNbO_3$, $\Gamma_{\mathrm{su}}$is $-0.045$ [Fig. 4(a)]. Thus, $\Gamma_m$ is calculated to be $-0.057$j. Similarly, the electrical reflection can be calculated as [31]

$$\Gamma_e = \Gamma_{0\infty} e^{j\alpha} \frac{1 - e^{-j2\alpha}\left(1 - \Gamma_{0\infty}^2\right)}{1 - \Gamma_{0\infty}^2 e^{-j2\alpha}} \tag{5}$$

where $\Gamma_e$ is the electrical reflection coefficient at the reflection center, $\Gamma_{0\infty}$ is the reflection coefficient due to the phase velocity difference in the metalized and free piezoelectric surfaces. $\Gamma_{0\infty}$ is obtained from COMSOL FEA eigenmode simulation

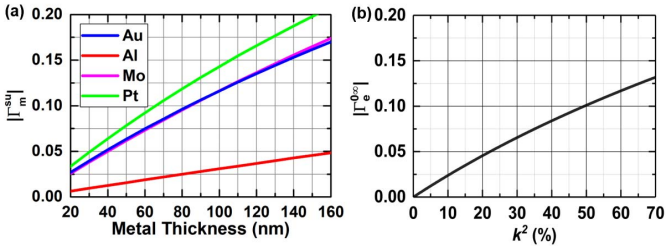


Fig. 4. Mechanical and electrical reflection coefficient caused by the interface between the $LiNbO_3$ film with and without electrode. The values are obtained using COMSOL FEA in the frequency domain.

of a piezoelectric slab with the electrically open or short surface boundary condition. Note that the electrodes are assumed massless. The relationship of the reflectivity to metal electrode thickness and metal type of the SPUDT has been recently examined and can be found in [31]. For the S0 mode with $\lambda$ of 6.4 $\mu$m in an 800 nm in $LiNbO_3$ film, $\Gamma_{0\infty}$ is $-0.0743$ [Fig. 4(b)], and thus $\Gamma_e$ is calculated to be $-0.105$j.

The comprehensive reflection coefficient $\Gamma_\lambda$, including the effects of mechanical and electrical reflections, can be calculated through the multireflection theory and expressed as [31]

$$\Gamma_\lambda = \frac{\Gamma_m + \Gamma_e}{1 + \Gamma_m \cdot \Gamma_e}. \tag{6}$$

The total reflection coefficient per reflector is calculated to be $-0.16$j, which is significantly larger than those obtained in SAW devices with a similar electrode thickness [23]. The large reflectivity is collectively caused by a higher $\Gamma_e$ from a larger $k^2$ and a higher $\Gamma_m$ from the more substantial electrode mass loading on a suspended thin film. Based on (3), the forbidden region caused by the limit on reflectivity is illustrated in gray in Fig. 3(b).

Upon comparing Fig. 3(a) with (b), it is evident that the S0 mode platform allows access to more favorable FBW-IL trade space and overcomes the fundamental performance limits of the SAW. Combined with their better energy confinement in the suspended structure and consequently lower PL, S0 ADLs can potentially enable wider BW and lower loss performance at the gigahertz frequency range. Note that the currently predicted performance is still far from harnessing the full potential of the S0 mode platform as the attained reflectivity is still the performance bottleneck and can be overcome in future optimizations.

### C. Simulation and Design of Key Parameters

To better capture the intricacies and understand the frequency-domain responses, we use COMSOL FEA for validating the S0 ADL prototype designs. To demonstrate the design fundamentals of the S0 ADLs, simplified 2-D simulations are used in Sections II-C and II-D of this section, assuming that the acoustic waves are plane waves and the fridge effects near the release windows can be neglected. The 3-D simulation results will be analyzed in Section II-E, emphasizing the propagation characteristics of the S0 mode acoustic waves in our proposed structure. The 2-D simulation is set up as follows. A slab of the proposed structure (Fig. 2) is modeled

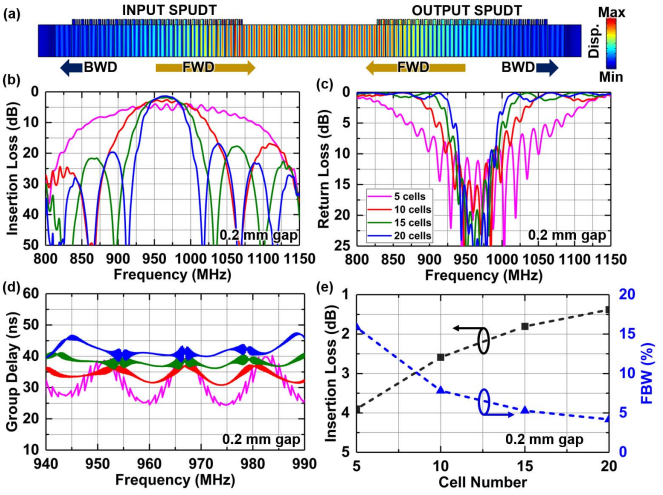


Fig. 5. Simulated performance of the gigahertz S0 ADLs with a 6.4-$\mu$m cell length, the same gap length of 0.2 mm, but different numbers of SPUDT cells (5–20). (a) Cross-sectional mode shape depicting the unidirectionality of the SPUDT transducers for an ADL with 20 cells and a gap length of 0.1 mm. The thickness of the cross section is exaggerated. (b) IL. (c) RL. (d) Group delay. (e) Extracted IL and FBW, illustrating their tradeoff.

in COMSOL, with the interdigitated electrodes (IDTs) but not the bus line parts [Fig. 5(a)]. Periodic boundary conditions are applied to the transverse edges for both the mechanical and electrical domains [46]. The 2-D simulation also assumes the whole structure, including the acoustic waveguide, to be lossless, given that PL remains unknown for S0 mode waves at these frequencies. PL will be experimentally derived in our measurement section. Perfectly matched layers (PMLs) are applied to both ends of the ADL.

First, we investigate the designs with different numbers of transducer cells, but the same gap length (0.2 mm), to determine the number of cells in our design for the SIC application. In the simulation, without loss of generality, the cell length is chosen to be 6.4 $\mu$m. Considering our in-house fabrication capabilities (more details will be discussed in Section III), the film stack is set as 135-nm-thick aluminum interdigitated transducers on the top of a suspended 800-nm $LiNbO_3$ thin film, As shown in the simulated cross-sectional mode shape [Fig. 5(a)], the SPUDTs on both ends significantly reduce the energy leakage to the BWDs. The simulated IL and RL are shown in Fig. 5(b)–(c) with the ports conjugately matched. For a device with 20 cells, an IL of 1.3 dB and a 3-dB FBW of 4.2% are expected, while an IL of 3.9 dB and an FBW of 16% are obtained for a device with five cells. The tradeoff between IL and FBW for our ADL platform is shown in Fig. 5(e). The simulation results indicate a substantially improved trade space that can lead to record-breaking low IL over a broad BW. For providing delays for SIC, we prioritize on providing low IL for adequately wide FBW. Based on the previous demonstration of SIC [47], we select 4% FBW (20 cells) as our primary design prototype. The simulated group delays are shown in Fig. 5(d). Delays from 25 to 45 ns are obtained with longer delays induced by longer acoustic wave propagation distances in devices with more cells. The ripples in delay are likely caused by the multireflection between the transducers. The absolute

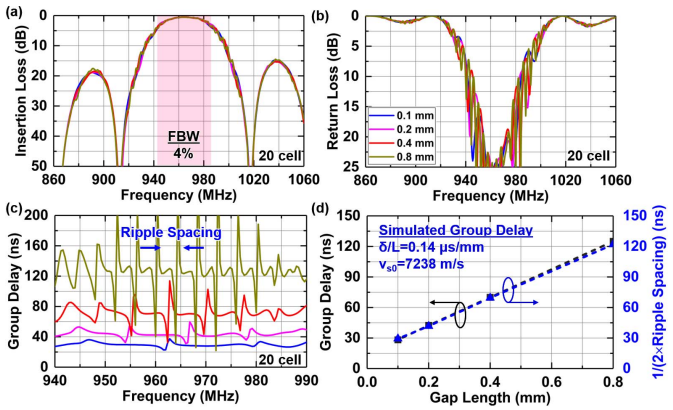


Fig. 6. Simulated performance of the gigahertz S0 ADLs with 6.4-$\mu$m cell length, the same number of SPUDT cells of 20, but different gap lengths varying from 0.1 to 0.8 mm. (a) IL. (b) RL. (c) Group delay. (d) Extracted group delay and the frequency spacings between the ripples, showing that the multireflections due to finite directionality are the source of the ripples in the group delay.

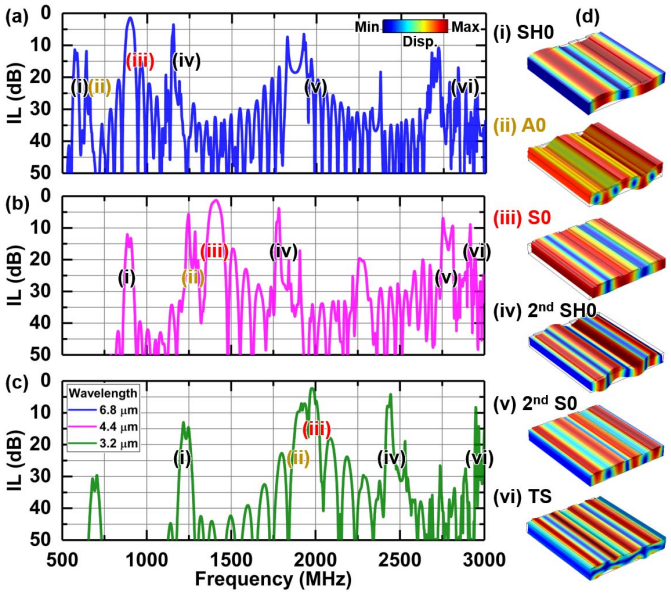


Fig. 7. (a)–(c) Simulated performance of the gigahertz S0 ADLs with different center frequencies. Different devices have the same number of SPUDT cells of 20, the same gap length of 0.1 mm, but different cell length varying from 6.8 to 3.2 $\mu$m. (d) Main passbands are identified for each case and the mode shape of each mode is shown.

delay value and the origin of the ripples will be discussed in the next paragraph.

Second, we study the effects of the gap length by simulating designs with the same number of cells (20) but different gap lengths varying from 0.1 to 0.8 mm. The study allows insights inaccurate prediction of the delays of different designs. The other critical parameters of the simulated structure remain the same as the previous group of ADLs. The simulated performance is shown in Fig. 6 with the ports conjugately matched. It can be seen that an IL around 1.1 dB and an FBW approximately 4.2% are obtained for different devices with various gap lengths [Fig. 6(a) and (b)], due to the lossless nature of the simulation setup. The simulated group delay is shown in Fig. 6(c). It is evident that devices with more considerable delay lengths lead to longer delays, as summarized in Fig. 6(d). The group delay $\tau$ can be approximated as

$$\tau \approx (L_g + N \cdot \lambda)/v_o \tag{7}$$

where $L_g$ is the gap length, $N$ is the cell number, $\lambda$ is the cell length, and $v_o$ is the phase velocity of S0 mode in $LiNbO_3$ thin film with the electrically open-surface boundary condition. As shown in Fig. 6(d), the extracted $v_o$ is 7238 m/s, which is equivalent to providing 0.14 $\mu$s/mm in S0 ADLs. Another observation is that the frequency spacing between ripples is smaller for more extended devices. Upon analyzing the frequency spacing quantitatively [Fig. 6(d)], the relation between the ripple spacing $\Delta f_{\text{sp}}$ and the delay $\tau$ can be summarized as

$$\Delta f_{\text{sp}} \approx \frac{1}{2\tau}. \tag{8}$$

Such a conclusion supports that the ripples are caused by the highly partial standing waves (with low standing wave ratio) formed between the two sets of transducers on opposite ends [23]. However, such effects are less severe in the previously demonstrated SH0 ADLs on the suspended $LiNbO_3$ thin films [1], [31]. The more subdued ripples are mainly a result of the higher damping of SH0 acoustic waves, which significantly lowers the quality factor $Q$ of such a mode and mitigates the local group delay fluctuations.

In this section, we have studied the key parameters of S0 mode ADLs, namely, the number of cells and the gap width. The simulations have shown the target performance of S0 ADLs for SIC applications, validating the greatly enhanced design space of the new platform. However, as it will be shown in Section II-D, scaling S0 ADLs toward the gigahertz range is not merely reducing the cell length, which is the same as the S0 mode wavelength. The presence of other spurious modes creates new challenges for attaining high-performance gigahertz ADLs.

### *D. Scaling S0 Mode Acoustic Delay Lines Toward Gigahertz*

To illustrate the challenges of scaling S0 ADLs toward higher frequencies, a group of devices with the same gap length (0.1 mm) and number of cells (20), but different cell lengths (6.4 to 3.2 $\mu$m) is simulated using FEA for an 800-nm film. The simulation results are shown in Fig. 7 with port impedance conjugately matched for the S0 mode. Six significant modes exist in the interested frequency range from 500 to 3000 MHz, creating a passband from each mode. As presented in Fig. 7(d), different modes are identified with the displacement mode shapes obtained from FEA. It is not surprising that the center frequencies of different bands scale up with shorter cell lengths. However, as highlighted in Fig. 7, the spacing between the S0 and A0 modes significantly reduced for higher frequency ADLs. In the case of a 3.2-$\mu$m cell length on the 800-nm thin film [Fig. 7(c)], the S0 and A0 passbands merge. In the overlapped passband, both the IL and RL degrade because part of the signal is coupled into the low $k^2$ A0 mode and travels at a different group velocity.

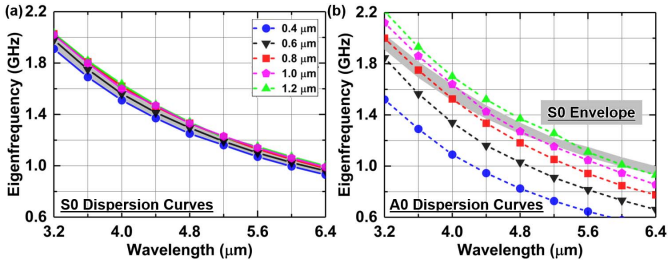


Fig. 8. Dispersion curves of (a) S0 mode and (b) A0 mode with different wavelengths in the $LiNbO_3$ thin films with various thicknesses. A0 is influenced more by the film thickness than S0. When the A0 dispersion curves become close to the S0 mode, the available FBW of the S0 mode is greatly reduced.

It thus cannot be adequately reflected by the embedded reflectors designed for S0 to achieve unidirectionality in the SPUDT transducers, resulting in more loss that is absent in nonoverlapping cases. Such a mode overlapping phenomenon significantly limits the available BW of the S0 ADL. To avoid the detrimental effect of overlapping the S0 and A0 passbands, thorough examinations on the dispersion curves of the S0 and A0 models are carried out to identify a mitigation approach.

The dispersion curves of S0 and A0 mode in a transducer cell are presented in Fig. 8 for $LiNbO_3$ films with different thicknesses. The curves are obtained using eigenmode FEA on a single cell with periodic boundary conditions in both the electrical and mechanical domains. As shown in Fig. 8(a), reducing the wavelength from 6.4 to 3.2 $\mu$m results in the increase of the center frequency of the S0 mode from 1 to 2 GHz. Moreover, the dispersion curves of the S0 mode show a weak dependence on the thickness-to-wavelength ratio [44]. For our specific cases, a thicker film leads to a higher compound phase velocity in the transducer. The dispersion curves of the A0 mode also show a similar trend, that is, a shorter wavelength and a thinner film lead to a lower center frequency [Fig. 8(b)]. The S0 mode dispersion curves are plotted on the same figure, showing a significant overlapping of both modes for certain film thickness. It can be seen that a thinner film provides a much larger space for scaling up the operating frequency. However, it is nontrivial to microfabricate the long ADLs (length up to several millimeters for adequate delays) on thin films. Therefore, it requires holistic consideration of the attainable operating frequency and the in-house fabrication capabilities. We select an 800-nm-thin film for demonstrating S0 ADL prototypes between 1 and 2 GHz in this work. Note that it is feasible to scale the S0 ADLs to even higher frequencies based on the recent advancement in processing low residue stress thin films of a reduced thickness [48].

### *E. Propagation of S0 Mode Acoustic Wave*

This section has been so far based on the plane wave simplification. This assumption is only valid when the launched acoustic waves propagate perfectly perpendicular to IDTs in the cut plane and do not have a wave vector component along the transverse direction. In other words, it requires the wavefront propagates in alignment with the energy transportation

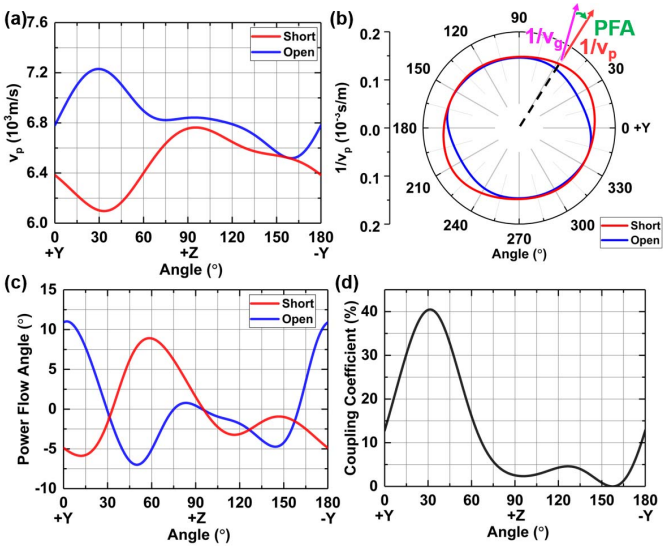


Fig. 9. S0 mode propagation characteristics in an X-cut $LiNbO_3$ film around 1 GHz. (a) Phase velocities of the S0 waves in an electrically open $LiNbO_3$ thin film ($v_o$) and an electrically short $LiNbO_3$ thin film ($v_s$). (b) Slowness curves of the S0 mode in electrically open and short $LiNbO_3$ thin films. (c) Calculated power flow angle. (d) Calculated coupling coefficient $k^2$ of S0.

direction [49]. Therefore, it is necessary to examine these two wave propagation directions in an actual ADL structure.

The wavefront propagation direction can be shown to be the same as that of the phase velocity $\boldsymbol{v_p}$, which is described as [50]

$$\boldsymbol{v_p} = \hat{\boldsymbol{k}}\omega/|\boldsymbol{k}| \tag{9}$$

where $\omega$ is the angular frequency, $\boldsymbol{k}$ is the wave vector, and $\hat{\boldsymbol{k}}$ is the unit vector of $\boldsymbol{k}$. The energy transportation direction can be generally proved as the same direction as the group velocity $\boldsymbol{v_g}$ of acoustic waves [51], which is described as [50]

$$\boldsymbol{v_g} = \vec{\nabla}_k \omega \tag{10}$$

which means the gradient of the angular frequency $\omega$ as a function of the wave vector $\boldsymbol{k}$. The angle between $\boldsymbol{v_p}$ and $\boldsymbol{v_g}$ is defined as the power flow angle (PFA), pointing from $\boldsymbol{v_g}$ to $\boldsymbol{v_p}$. PFAs of acoustic waves are not always zero for anisotropic materials, such as $LiNbO_3$ used for our ADLs [49]. If PFA is nonzero, the launched acoustic waves might propagate into the busline regions (Fig. 2) when reaching the other end, and be missed by the receiving IDTs. As a result, it might introduce additional IL to the actual devices than that predicted by the 2-D simulation (Figs. 5 and 6). Therefore, we need to examine the PFA for the S0 mode in X-cut $LiNbO_3$ to identify an in-plane orientation, at which large $k^2$ and adequately small PFA can be accessed simultaneously.

The slowness curve method developed for various acoustic applications [14] is used in this work for calculating PFA for Lamb waves in thin piezoelectric films [49]. The slowness curve is traced by the locus of the vector that is defined as the inverse of the phase velocity over the in-plane orientations [Fig. 9(b)]. The phase velocity direction of the S0 mode propagating along a given in-plane orientation coincides with

the radial vector pointing along the in-plane Euler angle. The direction of the group velocity is normal to the slowness curve for all in-plane orientations, as shown in Fig. 9(b) [49], therefore leading to the PFA.

For our case, we start with calculating the phase velocities $v_p$ of the S0 mode in X-cut $LiNbO_3$ at different in-plane orientations. We choose the S0 mode with 6.4-$\mu$m wavelength in an 800-nm-thin film as the example. COMSOL eigenmode FEA is used for obtaining the phase velocities of the electrically open $LiNbO_3$ thin film ($v_o$) and electrically short $LiNbO_3$ thin film ($v_s$) at different in-plane orientations [Fig. 9(a)]. A phase velocity around 6500 m/s is obtained for the S0 mode in our film stack. $v_s$ is slower than $v_o$ due to the piezoelectric softening effect [42]. Next, the slowness curves for different boundary conditions are plotted in Fig. 9(b) with an example of PFA presented. Using the aforementioned method, PFA curves at different in-plane orientations for both boundary conditions are plotted in Fig. 9(c). Targeting the high $k^2$ of the S0 mode in X-cut $LiNbO_3$, we investigate the PFA zero points near 30° to the $+y$-axis [Fig. 9(d)] [42], [43]. In the electrically open case, PFA reaches zero when the propagation direction is 29.5° to the $+y$-axis. For the electrically short case, PFA reaches zero at a propagation direction of 33.2° to the $+y$-axis. Deviation from these angles causes a nonzero PFA and a misalignment between the propagating acoustic wave and the receiving transducer direction, which degrades the device performance. Moreover, the suspended structure itself introduces more multireflections within the IDTs and between the etched transverse edges. Therefore, we use FEA to analyze the effects.

To better illustrate the effects of a nonzero PFA, two groups of S0 ADLs with different in-plane orientations are simulated with COMSOL FEA (Fig. 10). In the 3-D model, the total width of the device is 86 $\mu$m. The aperture width, defined as the overlap length between the blue and yellow electrodes in Fig. 2, is 50 $\mu$m. The other key dimensions are the same as those for the 2-D simulation in Fig. 6. The mechanical boundary conditions in the transverse direction are set to be free, while PMLs are used at the two ends in the longitudinal direction. For devices orientated 30° to the $+y$-axis [Fig. 10(a)], the displacement mode shape shows that most of the power still propagates toward the receiving transducer [Fig. 10(c)] due to the small PFA of $-0.27°$ at this orientation. In comparison to the results obtained from the 2-D simulation (Fig. 6), the slight degradation of IL for longer devices is due to the minor wave scattering into the bus line area where no IDTs are present to effectively collect the power carried by the waves. In contrast to devices orientated 30° to the $+y$-axis, devices orientated 35° to the $+y$-axis [Fig. 10(b)] show a significant direction deviation in energy transportation as seen from the displacement mode shape [Fig. 10(c)] due to a larger PFA of $-2.88°$. The launched acoustic waves thus impinge upon the transverse free boundaries of the suspended thin film and follow a reflection-induced zig-zag path down the waveguide. Interestingly, due to the existence of the transverse free boundaries, a longer device can potentially perform better than a shorter one, e.g., the 1.8-mm device in Fig. 10(b), if the bounced waves coincidentally get collected by the output

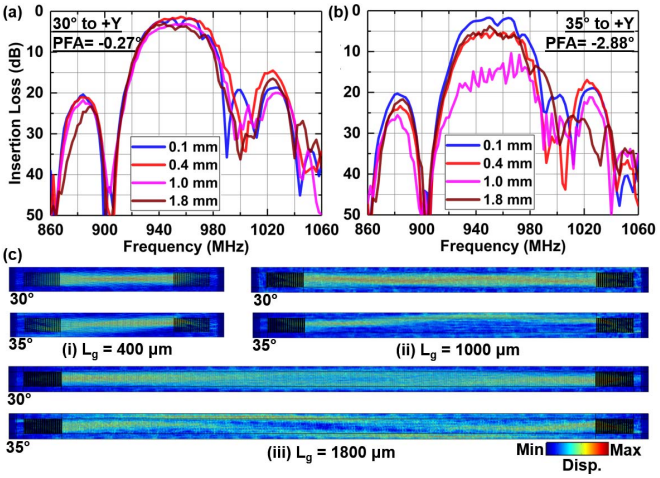


Fig. 10. Simulated effects of a nonzero PFA on ADL performance. The transmission coefficients (conjugately matched) for two groups of S0 ADLs with different in-plane device orientations at (a) 30° to $+y$-axis with a PFA of $-0.27°$ and (b) 35° to $+y$-axis with a PFA of $-2.88°$. (c) Displacement mode shapes for devices at different orientations and PFAs. A larger deviation from the zero PFA leads to a larger IL for certain gap widths as the guided acoustic waves might miss the output transducers in their zig-zag paths.

transducer. Nonetheless, to avoid complications and consistently attain low IL for different lengths, it is crucial to align the devices to the zero PFA orientation as close as possible. It is also noteworthy that the PFA issue can be potentially mitigated using slanted transducers, which were developed for aligning the energy flow angle with the transducers for various SAW applications [52], [53].

To sum up, we have explored the design space for gigahertz S0 mode ADLs in this section. First, the significantly improved FBW-IL trade space is theoretically shown in the new platform, promising superior gigahertz ADLs for SIC applications. Next, the design of S0 SPUDT is presented, with the two key parameters, namely, the number of cells and gap length, explored for determining the center frequency, IL, FBW, and delay of the ADLs. The challenges in scaling S0 ADLs to higher frequencies have been identified, and an approach considering both the targeting frequencies and fabrication process has been developed. Finally, we investigate the S0 mode propagation properties in the ADL and discuss a potentially critical design parameter, device in-plane orientation, for long delays and minimum IL degradation at the same time. The device implementation will be presented in Section III.

## III. Acoustic Delay Line Implementation

The devices were in-house fabricated with the process shown in Fig. 11. The X-cut $LiNbO_3$ thin film of 800 nm on a 4-in Si wafer is provided by NGK Insulators, Ltd., for this fabrication process. First, the electrodes are defined with e-beam lithography to create feature sizes as small as 400 nm. Then, 135-nm-thick aluminum electrodes are patterned using sputtering and lift off. Aluminum is chosen for its good conductivity for lowering the electrical loss and also its compatibility with the follow-on steps. The thickness of the electrodes is chosen within the limit of our e-beam photoresist-based lift-off process. Next, a 2-$\mu$m $SiO_2$ layer

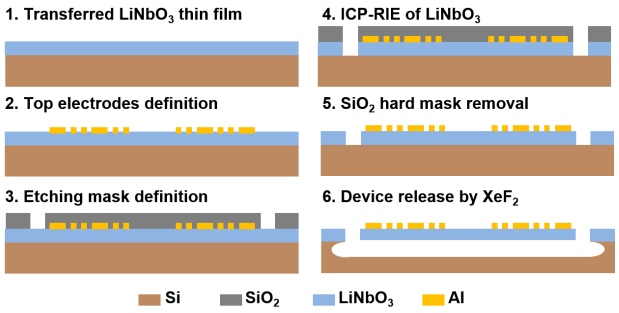


Fig. 11. Fabrication flowchart of the gigahertz S0 ADLs.

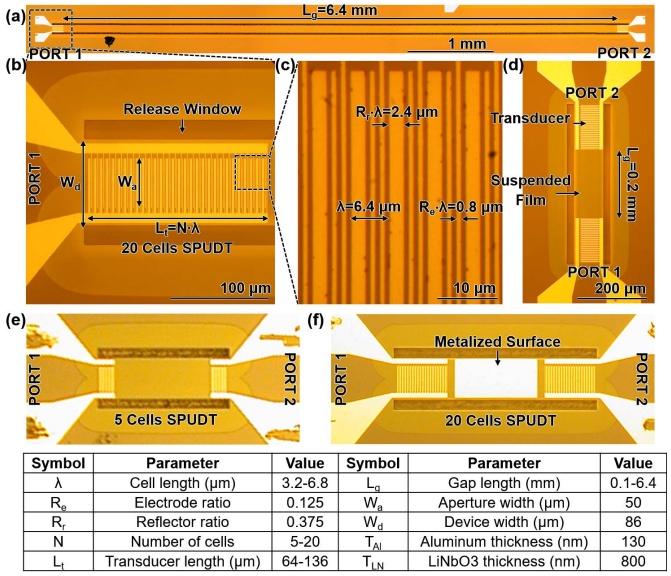


| Symbol | Parameter | Value | Symbol | Parameter | Value |
|---|---|---|---|---|---|
| λ | Cell length (μm) | 3.2-6.8 | $L_g$ | Gap length (mm) | 0.1-6.4 |
| $R_e$ | Electrode ratio | 0.125 | $W_a$ | Aperture width (μm) | 50 |
| $R_r$ | Reflector ratio | 0.375 | $W_d$ | Device width (μm) | 86 |
| N | Number of cells | 5-20 | $T_{Al}$ | Aluminum thickness (nm) | 130 |
| $L_I$ | Transducer length (μm) | 64-136 | $T_{LN}$ | LiNbO3 thickness (nm) | 800 |

Fig. 12. Optical microscope images of the fabricated ADLs. (a) Zoomed-out, (b) transducer, and (c) zoomed-in views of the longest fabricated device with a 6.4-mm gap. (d) Shorter device with a 0.2-mm gap. (e) Five-cell SPUDT test device for validating the effects of cell numbers. (f) Test structure for identifying the PL in a metalized $LiNbO_3$ thin film. The key parameters are shown in the inset table.

is deposited using plasma-enhanced chemical vapor deposition (PECVD) and patterned with fluorine-based reactive ion etching (RIE). The release windows in the $LiNbO_3$ film are subsequently etched using chlorine-based inductive coupled plasma (ICP)-RIE. The remaining $SiO_2$ is then removed with low-power ICP. Finally, the ADLs are released with isotropic $XeF_2$ etching. In this process, the diced sample has a side aligned with the $+y$-axis of the $LiNbO_3$ material. The device orientation is preset in the lithography mask with each device tilted 30° to the reference $+y$-axis on the mask. In the implementation, the reference axis on the mask is aligned to the side of the sample that was aligned with the $+y$-axis of the $LiNbO_3$ crystal.

The optical images of the fabricated ADLs are shown in Fig. 12 with the critical parameters marked in the figures. The longest fabricated device features a high aspect ratio (total length/aperture width) of 128 and displays no visible warping under a microscope [Fig. 12(a)], demonstrating adequate stress management in the fabrication. The SPUDT electrodes are

TABLE I

KEY PARAMETERS OF THE FABRICATED DEVICES

| Index | Cell Length (μm) | Gap Length (mm) | No. of Cells | Sim. (Fig.) | Meas. (Fig.) | Comments |
|---|---|---|---|---|---|---|
| Group A | 6.4 | 0.2 | 5-20 | 5 | 13 | No. of cells |
| Group B | 6.4 | 0.2 – 6.4 | 20 | 6 | 14 | Gap length |
| Group C | 3.2 – 6.8 | 0.1 | 20 | 7 | 15-16 | Cell length |
| Group D | 3.2 – 6.4 | 0.1 – 6.4 | 20 | - | 17 | PL at different frequencies |
| Group E | 5.2 | 0.1 – 1.6 | 20 | - | 18 | PL in metalized thin film |
| Group F | 6.4 | 0.2 – 6.4 | 20 | - | 19 | TCF, PL in vacuum |

also defined with high fidelity in width and great uniformity across cells [Fig. 12(b) and (c)]. Three key parameters of the ADL designs (number of cells, gap length, and cell length) are investigated individually. The number of cells varies from 5 to 20 [Fig. 12(e)]. The gap length varies between 0.1 and 6.4 mm [Fig. 12(d)], providing delays ranging from 20 to 900 ns. The cell length varies from 6.8 to 3.2 $\mu$m, covering center frequencies from 900 MHz to 2 GHz. Some test structures are also fabricated, aiming to investigate the PL of the metalized $LiNbO_3$ thin film. Most of the fabricated devices exhibit flat surfaces and well-defined electrodes from optical inspection and perform as anticipated. The orientation of the fabricated devices is optically identified to be 30.8° to the $+y$-axis. The slight deviation from 30° to the $+y$-axis was caused by the slight misalignment in the fabrication.

To fully break down the IL, attain empirical data on the PL of S0, and ultimately validate our understanding of the performance limits of ADLs, different groups of devices were fabricated. A summary of the fabricated devices is shown in groups from A to F in Table I. For easy references and comparisons, the figures showing the simulation and measurement results of these groups are also listed in Table I. Groups A and B are used for validating the key design parameters (number of cells and gap length) for determining the IL, FBW, and group delay. Group C is used for showing our approach to scale our lower frequency devices to the gigahertz frequency range. Groups D, E, and F are used to identify the PL of S0 mode at different conditions, which cannot be directly obtained by FEA.

## IV. MEASUREMENT AND DISCUSSIONS

### A. Acoustic Delay Lines With Different Cell Numbers

The fabricated ADLs were first measured with a vector network analyzer (VNA) at the −10-dBm power level in the dry air, and then conjugately matched in Keysight Advanced Design System. The devices in Group A are designed to investigate the impact of the number of cells on the IL-FBW tradeoff. Devices with the same cell length of 6.4 $\mu$m and the same gap length of 0.2 mm, but different numbers of SPUDT cells of 5, 10, and 20 were built. The measured IL and RL are shown in Fig. 13(a) and (b) with the ports conjugately matched. For a device with 20 cells, an IL of 3.2 dB and a 3-dB FBW of 3.8% are obtained, while for a device with

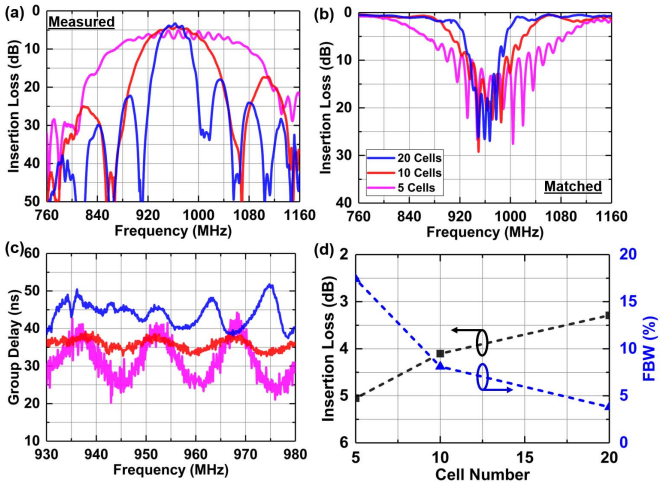


Fig. 13. Measured performance of the gigahertz S0 ADLs with the same 6.4-$\mu$m cell length, the same gap length of 0.2 mm, but different numbers of SPUDT cells (5–20). (a) IL. (b) RL. (c) Group delay. (d) Extracted IL and FBW, illustrating their tradeoff.

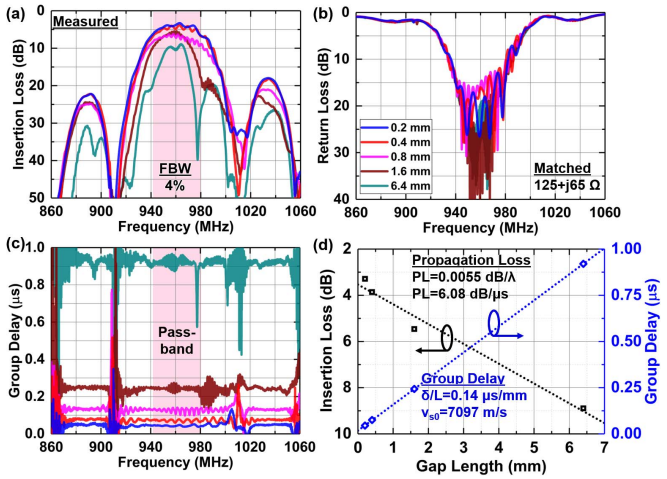


Fig. 14. Measured S-parameters of the ADLs ($N = 20$, $\lambda = 6.4$ $\mu$m) with identical transducers but different $L_g$ (0.2–6.4 mm). (a) IL and (b) RL responses showing an FBW of 4% and a minimum IL of 3.2 dB. (c) Group delay responses with the passband highlighted. (d) Extracted PL (6.08 dB/$\mu$s), and phase velocity (7097 m/s) of the S0 mode in $LiNbO_3$ at 960 MHz.

five cells, an IL of 5.0 dB and an FBW of 17.4% are shown. The tradeoff between IL and FBW for our ADL platform is shown in Fig. 13(d). Compared to the simulated results in Fig. 5(e), a slight degradation in IL has been observed, which will be analyzed in Section IV-D. The IL-FBW has been dramatically improved from the SOA SAW ADLs, therefore allowing access to the previously forbidden design space for low-loss wideband ADLs and the future SIC applications. The measured group delays are shown in Fig. 13(c). Delays from 25 to 45 ns are obtained, with longer delays induced by longer transducers with more cells. The frequency spacing between the adjacent ripples is inversely proportional to the group delay, as expected in Fig. 6. The larger ripples in both the amplitude and the group delay of the ADLs with fewer cells are caused by the insufficient suppression of triple travel signals (TTSs) from the less unidirectionality in the transducers.

### *B. Acoustic Delay Lines With Different Gap Lengths*

The devices in Group B are designed to investigate the effects of longer gap lengths. This group includes ADLs with identical transducers ($\lambda = 6.4$ $\mu$m) but different gap lengths (0.2–6.4 mm). The performance shows an FBW of 4% and a minimum IL of 3.2 dB [Fig. 14(a) and (b)]. Group delays between 40 and 900 ns have been obtained for different gaps [Fig. 14(c)]. The small ripples in the IL and the group delays are collectively caused by the finite directionality of the transducers and the slight resonant nature of the SPUDT. The first aspect can be improved by enhancing the reflectivity per cell and achieving a further reduced TTS between the transducers [1], [23]. The second factor can be mitigated using the optimization approaches developed for SAW SPUDT devices [16], [54], [55], namely, optimizing the reflection and transduction functions simultaneously across the transducer.

The IL of ADLs with different lengths is further analyzed. Naturally, the IL increases for longer delays, which is commensurate with the more damped signals reflected from a further distance in the SIC scheme. The extracted PL in the dry air ambiance and phase velocity is 6.08 dB/$\mu$s and 7097 m/s, respectively [Fig. 6(d)]. Note that the PL extracted here is a conservative estimation, because the longer devices with a high aspect ratio over 128 suffer from the nonzero PFA issue (even for a small PFA) explained in Section II. Fortunately, the etched transverse free boundaries help to confine the energy in the propagation path. Approaches to further reduce the PFA issue will be explored in our future work.

### *C. Acoustic Delay Lines With Different Center Frequencies*

The Group C ADLs have the same gap length of 0.1 mm but different transducers ($\lambda = 3.2$–$6.8$ $\mu$m). The wideband measurement results are shown in Fig. 15. The transmission at higher frequencies has the same trend regarding S0 and A0 modes as predicted by the simulation (Fig. 7). For our 800-nm-thick 20 cell $LiNbO_3$ ADLs, the S0 passband shows good performance up to 2 GHz. Various transducer wavelengths result in passbands ranging from 0.8 to 2 GHz with FBWs around 4% [Fig. 16(a) and (b)]. An IL of 3.0 dB is achieved for the 900-MHz ADL, while an IL of 5.2 dB is attained for the 2-GHz ADL. The slightly larger IL for higher frequency ADLs is caused by the larger electrical length for a given $L_g$ at a higher frequency and the constant PL/$\lambda$empirically observed over the said frequency range. As shown in Fig. 16(c), a delay as low as 20 ns has been demonstrated over the 0.8–2-GHz range. The slight ripples in the group delay are caused by the multireflections in SPUDTs.

### *D. Gigahertz S0 Wave Propagation in Thin Film*

The propagation characteristics of S0 waves in $LiNbO_3$ thin film are further investigated. The devices with different cell

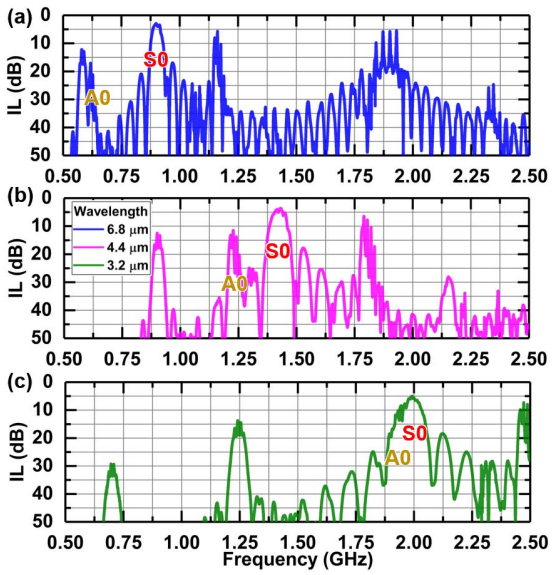


Fig. 15. Measured performance of the gigahertz S0 ADLs with different center frequencies. The devices have the same number of SPUDT cells of 20, the same gap length of 0.1 mm, but different cell lengths [(a) 6.8, (b) 4.4, and (c) 3.2 $\mu$m].

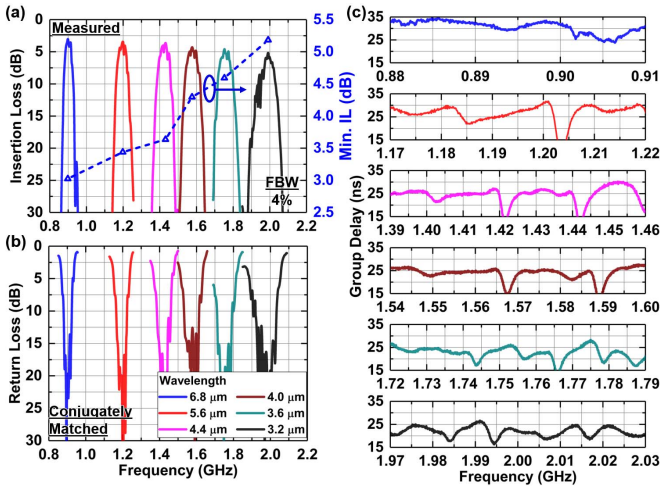


Fig. 16. Measured S-parameters of the ADLs ($N = 20$, $L_g = 0.1$ mm) with identical gap lengths but different $\lambda$ (3.2–6.8 $\mu$m) or center frequencies. (a) IL and (b) RL responses showing an FBW of 4% at different frequencies. (c) Measured group delays of different ADLs in the passbands, showing a minimum delay of 20 ns.

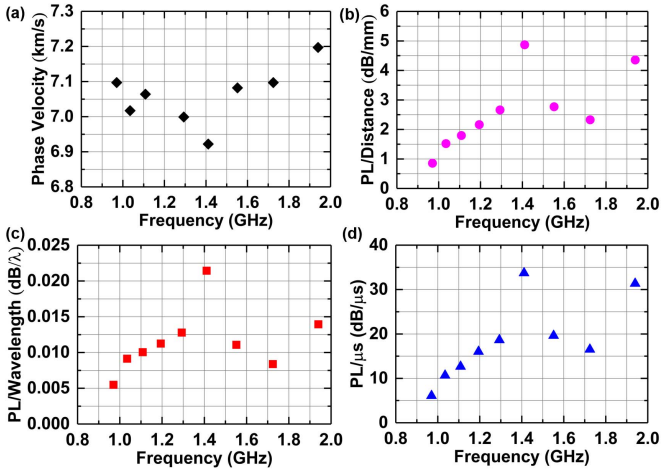


Fig. 17. Extracted propagation parameters of the gigahertz $S_0$ mode acoustic waves. (a) $v_o$, (b) PL per distance, (c) PL per wavelength, and (d) PL per microsecond.

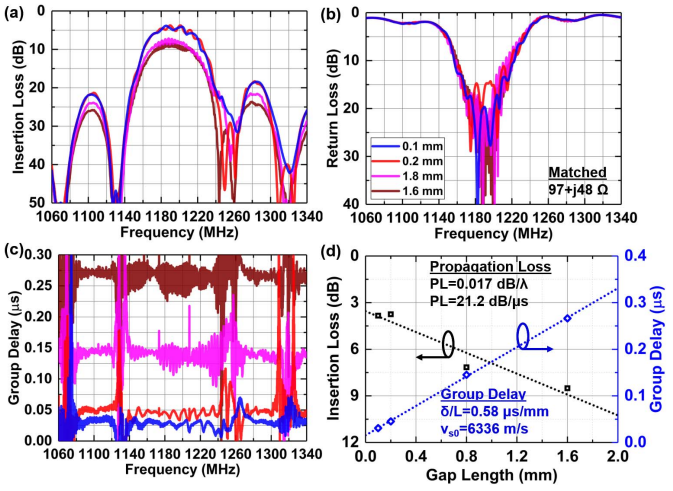


Fig. 18. Measured S-parameters of the ADLs ($N = 20$, $\lambda = 5.2$ $\mu$m) with identical transducers but different $L_g$ (0.1–1.6 mm) covered with 135 nm of Al. (a) IL. (b) RL. (c) Group delay. (d) Extracted PL (6.08 dB/$\mu$s), and phase velocity (7097 m/s) of the S0 mode at 1180 MHz in a $LiNbO_3$ thin film with a metalized surface.

lengths were fabricated and measured (Group D in Table I). The phase velocity $v_o$ and PL are extracted from devices with different gap lengths. The extracted $v_o$ is shown in Fig. 17(a) with a constant value around 7000 m/s over the 1–2-GHz range in the 800-nm-thin film. The PL at different frequencies is shown in Fig. 17(b)–(d) using three metrics, including PL per unit distance, PL per wavelength, and PL per unit time. Due to the nonzero PFA, the PL extracted here is a conservative estimation. The longer devices in this group suffer additional IL due to the transverse propagation of S0 waves (Fig. 10). Therefore, the PL extracted here is worse than the real cases. An increase of PL can be observed at higher frequencies, which is consistent with the experimental trends seen in various other acoustic device platforms [33], [56]–[58]. More holistic and sophisticated modeling on PL is still being developed as the research community gains more experimental insights on the critical factors affecting PL and better control of fabrication variations. Designs that better isolate the PL from other loss mechanisms (e.g., nonzero PFA) can also help to enable a more thorough analysis and will be our target in future work.

Next, the propagation characteristics of S0 waves in $LiNbO_3$ thin film with the metalized surface are extracted for understanding the PL in the transducer cells where the metalized thin film might be the main damping contributor [13]. A group of devices (Group E) centered at 1185 MHz was measured [Fig. 18(a)–(c)]. The extracted key parameters are shown in Fig. 18(d). Due to the piezoelectric softening effect [15], the phase velocity is lower than that measured in an electrically

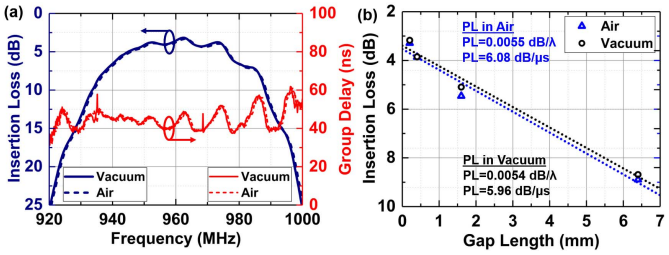


Fig. 19. Comparison of the measured IL and group delays of the S0-mode ADLs in vacuum and in air. (a) IL and group delay of an ADL ($N = 20$, $\lambda = 6.4$ $\mu$m, $L_g = 0.2$ mm) measured in vacuum and air. (b) PL in vacuum extracted from a group of ADLs ($N = 20$, $\lambda = 6.4$ $\mu$m, $L_g = 0.2$–$6.4$ mm, Group F in Table I).

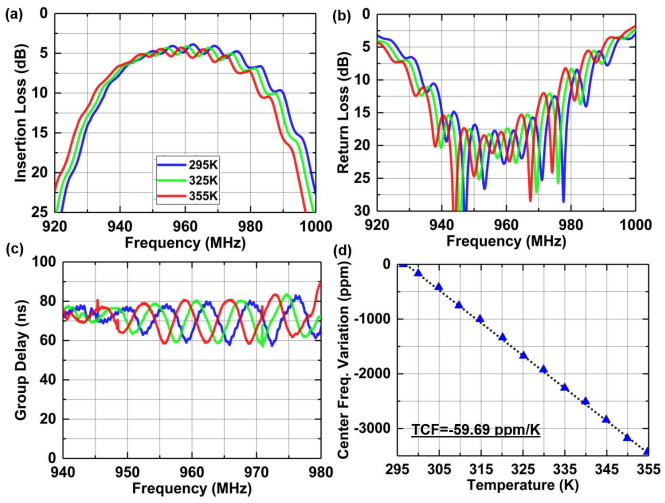


Fig. 20. Measured temperature dependence of an ADL ($N = 20$, $\lambda = 6.4$ $\mu$m, $L_g = 0.2$ mm) in vacuum. (a) IL. (b) RL. (c) Group delay at different temperatures is presented. (d) Center frequency variation and the extracted TCF in the frequency range of 295–355 K are shown.

open piezoelectric thin film. The measured $v_s$ is 6336 m/s. The extracted PL is 0.0017 dB/$\lambda$ or 21.2 dB/$\mu$s, which is much larger than the values in the electrically open thin film. Such a result implies that the metalized area is the main contributor of the IL in the transducer sections of the ADLs [31].

At last, the devices in Group F were then measured in vacuum for testing the effects of vacuum ambiance on the device performance. The results are presented in Fig. 19(a) for an ADL [$N = 20$, $\lambda = 6.4$ $\mu$m, $L_g = 0.2$ mm, Fig. 12(d)]. The different measurement environment brings little difference to the performance. The PL of these devices measured in air and vacuum is then compared in Fig. 19(b). The PL slightly drops from 6.08 to 5.96 dB/$\mu$s. Therefore, it can be found that the air damping is not the main loss in ADLs.

### *E. Temperature Dependence of Gigahertz S0 Acoustic Delay Lines*

The temperature dependence is another important factor in SIC applications for covering the entire operating temperature range of the front-end modules. Therefore, one ADL in Group F is measured at different temperatures, ranging from 295 to 355 K. The conjugately matched results are shown in Fig. 20(a)–(c), with both the transmission, reflection, and group delay plotted. The passband drifts to lower frequencies due to the negative temperature coefficient of stiffness of the $LiNbO_3$ film. The temperature coefficient of the center frequency (TCF) is plotted in Fig. 20(d), showing a TCF around $-59.69$ ppm/K. The result shows good linearity over the measured frequency range. The TCF is close to the previously reported TCF in S0 mode X-cut $LiNbO_3$ devices [28], [59], [60]. The temperature coefficient of delay is challenging to extract accurately, due to the existence of ripples in the group delay measurements. Such an effect will be further investigated in future works based on ADLs with optimized amplitude and phase performance [16].

### *F. Insertion Loss Breakdown in Gigahertz S0 Acoustic Delay Lines*

Based on the FEA simulation that has been validated by our measurements and the experimental extracted results, the IL of the gigahertz S0 ADLs is broken down for identifying the space for future improvement (Table II).

TABLE II
EXAMPLES OF IL BREAKDOWN

| Damping Source | 0.2 mm ADL IL | 6.4 mm ADL IL |
|---|---|---|
| Finite Uni-directionality | 1.3 dB | 1.3 dB |
| PL in Transducers | 0.25 dB | 0.25 dB |
| PL in Waveguide | 0.17 dB | 5.5 dB |
| Others (Including Electrical Loading & Non-zero PFA) | 1.4 dB | 1.85 dB |
| Total | 3.2 dB | 8.9 dB |

A pair of ADLs in Group A is studied as examples, one with a 0.2-mm gap length [Fig. 12(d)] and the other one with a 6.4-mm gap length [Fig. 12(a)]. For the 0.2-mm ADL, the first damping contributor is the finite unidirectionality in the transducers. Based on the FEA of a lossless structure (Fig. 5), 1.3 dB is from such an effect. The second damping source is the PL in the transducers, which can be calculated from the extrapolated delay in the transducers and the PL in $LiNbO_3$ thin-film sections with and without electrodes. A total of 0.25 dB is due to the PL in the transducers. The third damping term is the PL in the waveguide between the transducers. For the 0.2-mm ADL, the loss is 0.17 dB. Finally, the last 1.4-dB IL might be collectively caused by the electrical loading of the IDTs [61] and the nonzero PFA [49]. Similarly, the IL breakdown of the 6.4-mm ADL is shown in the table, with the PL in the waveguide as the main loss contributor.

For future implementations of gigahertz S0 ADLs, several approaches can be taken for achieving better performance. First, thicker IDTs can be implemented. The current metal thickness is limited by our in-house fabrication capabilities. With a further optimized fabrication process, a thicker metal layer will lead to lower loss from the unidirectionality (not worse than 0.8 dB [1]) and less electrical loading [61]. Second, damping from nonzero PFA can be reduced by the more accurate alignment of the sample and a larger ratio of aperture width to device width. The last damping term due to electrical

loading and nonzero PFA might be reduced to half of the current value. Therefore, a sub-2-dB IL for a 0.2-mm ADL and a sub-7.5-dB IL for a 6.4-mm ADL can be expected in future implementations.

## V. Conclusion

In this work, we have demonstrated low-loss wideband gigahertz S0-mode ADLs. The significantly improved FBW-IL tradeoff of S0 ADLs compared with SOA has been shown theoretically. The critical design parameters of S0 ADLs, including cell number, gap length, and cell length, have been investigated through simulation. The main design difficulties for high-performance gigahertz ADLs, including the adjacent spurious modes and nonzero power flow angle, are identified and discussed for the first time. The fabricated miniature ADLs show an FBW of 4% and a minimum IL of 3.2 dB at a center frequency of 0.96 GHz. Various delays ranging from 20 to 900 ns have been obtained for digitally addressable delay synthesis. Multiple ADLs with center frequencies from 0.9 to 2 GHz have been demonstrated. The PL of the S0 mode at the gigahertz frequency range is also experimentally measured for the first time, showing a PL of 6.08 dB/$\mu$s at 0.96 GHz or 0.0055 dB/$\lambda$ (dB per wavelength). The PL at different frequencies, measured conditions, and electrical boundary conditions is experimentally extracted. The demonstrated ADLs can potentially provide wide-range and high-resolution reconfigurable delays for future SIC applications.

## Acknowledgment

The authors would like to thank Dr. T. Olsson for helpful discussions.

## References

[1] R. Lu, T. Manzameque, Y. Yang, and S. Gong, "S0-mode lithium niobate acoustic delay lines with 1 dB insertion loss," in *Proc. IEEE Int. Ultrason. Symp. (IUS)*, Kobe, Japan, Oct. 2018, pp. 1–9.

[2] D. Bharadia, E. McMilin, and S. Katti, "Full duplex radios," *ACM SIGCOMM Comput. Commun. Rev.*, vol. 43, no. 4, pp. 375–386, Oct. 2013.

[3] Z. Zhang, X. Chai, K. Long, A. V. Vasilakos, and L. Hanzo, "Full duplex techniques for 5G networks: Self-interference cancellation, protocol design, and relay selection," *IEEE Commun. Mag.*, vol. 53, no. 5, pp. 128–137, May 2015.

[4] S. Hong *et al.*, "Applications of self-interference cancellation in 5G and beyond," *IEEE Commun. Mag.*, vol. 52, no. 2, pp. 114–121, Feb. 2014.

[5] J. Zhou *et al.*, "Integrated full duplex radios," *IEEE Commun. Mag.*, vol. 55, no. 4, pp. 142–151, Apr. 2017.

[6] B. Lee, J.-B. Lim, C. Lim, B. Kim, and J.-Y. Seol, "Reflected self-interference channel measurement for mmWave beamformed full-duplex system," in *Proc. IEEE Globecom Workshops (GC Wkshps)*, Dec. 2015, pp. 1–6.

[7] X. Wu, Y. Shen, and Y. Tang, "The power delay profile of the single-antenna full-duplex self-interference channel in indoor environments at 2.6 GHz," *IEEE Antennas Wireless Propag. Lett.*, vol. 13, pp. 1561–1564, 2014.

[8] D. Liu, Y. Shen, S. Shao, Y. Tang, and Y. Gong, "On the analog self-interference cancellation for full-duplex communications with imperfect channel state information," *IEEE Access*, vol. 5, pp. 9277–9290, 2017.

[9] X. Guo, Z. Gong, Q. Zhong, X. Liang, and Z. Liu, "A miniaturized reconfigurable broadband attenuator based on RF MEMS switches," *J. Micromech. Microeng.*, vol. 26, no. 7, p. 74002, May 2016.

[10] F. Vecchi, M. Repossi, W. Eyssa, P. Arcioni, and F. Svelto, "Design of low-loss transmission lines in scaled CMOS by accurate electromagnetic simulations," *IEEE J. Solid-State Circuits*, vol. 44, no. 9, pp. 2605–2615, Sep. 2009.

[11] C. L. Grasse and D. A. Gandolfo, "Acoustic surface wave dispersive delay lines as high resolution frequency discriminator," in *Proc. Ultrason. Symp.*, Oct. 1972, pp. 233–236.

[12] L. Reindl *et al.*, "Design, fabrication, and application of precise SAW delay lines used in an FMCW radar system," *IEEE Trans. Microw. Theory Techn.*, vol. 49, no. 4, pp. 787–794, Apr. 2001.

[13] S. Lehtonen, V. P. Plessky, C. S. Hartmann, and M. M. Salomaa, "SPUDT filters for the 2.45 GHz ISM band," *IEEE Trans. Ultrason., Ferroelectr., Freq. Control*, vol. 51, no. 12, pp. 1697–1703, Dec. 2004.

[14] D. Morgan, *Surface Acoustic Wave Filters*. Amsterdam, The Netherlands: Elsevier, 2007.

[15] K. Hashimoto, *Surface Acoustic Wave Devices in Telecommunications: Modelling and Simulation*. Berlin, Germany: Springer-Verlag, 2013. [Online]. Available: https://www.springer.com/us/book/9783540672326#aboutBook

[16] J. M. Hode, J. Desbois, P. Difilie, M. Solal, and P. Ventura, "SPUDT-based filters: Design principles and optimization," in *Proc. IEEE Int. Symp. Ultrason.*, Nov. 1995, pp. 39–50.

[17] J. Devkota, P. Ohodnicki, and D. Greve, "SAW sensors for chemical vapors and gases," *Sensors*, vol. 17, no. 4, p. 801, 2017.

[18] A. Pohl, "A review of wireless SAW sensors," *IEEE Trans. Ultrason., Ferroelectr., Freq. Control*, vol. 47, no. 2, pp. 317–332, Mar. 2000.

[19] R. Lu, J. Krol, L. Gao, and S. Gong, "A frequency independent framework for synthesis of programmable non-reciprocal networks," *Sci. Rep.*, vol. 8, Oct. 2018, Art. no. 14655.

[20] R. Lu, T. Manzaneque, Y. Yang, L. Gao, A. Gao, and S. Gong, "A radio frequency nonreciprocal network based on switched acoustic delay lines," *IEEE Trans. Microw. Theory Techn.*, vol. 67, no. 4, pp. 1516–1530, Apr. 2019.

[21] R. Ruby, P. Bradley, D. Clark, D. Feld, T. Jamneala, and K. Wang, "Acoustic FBAR for filters, duplexers and front end modules," in *IEEE MTT-S Int. Microw. Symp. Dig.*, Jun. 2004, pp. 931–934.

[22] C. S. Hartmann, P. V. Wright, R. J. Kansy, and E. M. Garber, "An analysis of saw interdigital transducers with internal reflections and the application to the design of single-phase unidirectional transducers," in *Proc. Ultrason. Symp.*, Oct. 1982, pp. 40–45.

[23] C. S. Hartmann and B. P. Abbott, "Overview of design challenges for single phase unidirectional SAW filters," in *Proc. IEEE Ultrason. Symp.*, Oct. 1989, pp. 79–89.

[24] R. H. Olsson, III, *et al.*, "A high electromechanical coupling coefficient SH0 Lamb wave lithium niobate micromechanical resonator and a method for fabrication," *Sens. Actuators A, Phys.*, vol. 209, pp. 183–190, Mar. 2014.

[25] R. Lu, T. Manzaneque, Y. Yang, and S. Gong, "Exploiting parallelism in resonators for large voltage gain in low power wake up radio front ends," in *Proc. IEEE Micro Electro Mech. Syst. (MEMS)*, Jan. 2018, pp. 747–750.

[26] Y.-H. Song, R. Lu, and S. Gong, "Analysis and removal of spurious response in SH0 lithium Niobate MEMS resonators," *IEEE Trans. Electron Devices*, vol. 63, no. 5, pp. 2066–2073, May 2016.

[27] R. Wang, S. A. Bhave, S. Zhgoon, and K. Bhattacharjee, "Multi-frequency $LiNbO_3$ Lamb wave resonators with $< 3\Omega$ impedance," in *Proc. IEEE 29th Int. Conf. Micro Electro Mech. Syst. (MEMS)*, Jan. 2016, pp. 679–682.

[28] S. Gong and G. Piazza, "Design and analysis of lithium–niobate-based high electromechanical coupling RF-MEMS resonators for wideband filtering," *IEEE Trans. Microw. Theory Techn.*, vol. 61, no. 1, pp. 403–414, Jan. 2013.

[29] L. Colombo, A. Kochhar, G. Vidal-Álvarez, and G. Piazza, "X-cut lithium niobate laterally vibrating MEMS resonator with figure of merit of 1560," *J. Microelectromech. Syst.*, vol. 27, no. 4, pp. 602–604, Aug. 2018.

[30] R. Wang, S. A. Bhave, and K. Bhattacharjee, "Design and fabrication of $S_0$ Lamb-wave thin-film lithium niobate micromechanical resonators," *J. Microelectromech. Syst.*, vol. 24, no. 2, pp. 300–308, Apr. 2015.

[31] T. Manzaneque, R. Lu, Y. Yang, and S. Gong, "Low-loss and wideband acoustic delay lines," *IEEE Trans. Microw. Theory Techn.*, vol. 67, no. 4, pp. 1379–1391, Apr. 2019.

[32] T. Manzaneque, R. Lu, Y. Yang, and S. Gong, "An SH0 lithium niobate correlator for orthogonal frequency coded spread spectrum communications," in *Proc. Joint Conf. Eur. Freq. Time Forum IEEE Int. Freq. Control Symp.*, Jul. 2017, pp. 143–147.

[33] T. Manzaneque, R. Lu, Y. Yang, and S. Gong, "Lithium niobate MEMS chirp compressors for near zero power wake-up radios," *J. Microelectromech. Syst.*, vol. 26, no. 6, pp. 1204–1215, Dec. 2017.

[34] T. Manzaneque, R. Lu, Y. Yang, and S. Gong, "An SH0 Lithium Niobate dispersive delay line for chirp compression-enabled low power radios," in *Proc. IEEE 30th Int. Conf. Micro Electro Mech. Syst. (MEMS)*, Jan. 2017, pp. 155–158.

[35] R. Lu, T. Manzaneque, Y. Yang, J. Zhou, H. Hassanieh, and S. Gong, "RF filters with periodic passbands for sparse Fourier transform-based spectrum sensing," *J. Microelectromech. Syst.*, vol. 27, no. 5, pp. 931–944, Oct. 2018.

[36] R. Wang, K. Bhattacharjee, and S. A. Bhave, "Thin-film lithium niobate contour-mode resonators," in *Proc. IEEE Int. Ultrason. Symp.*, Oct. 2012, pp. 303–306.

[37] M. Kadota, T. Ogami, K. Yamamoto, H. Tochishita, and Y. Negoro, "High-frequency Lamb wave device composed of MEMS structure using $LiNbO_3$ thin film and air gap," *IEEE Trans. Ultrason., Ferroelectr., Freq. Control*, vol. 57, no. 11, pp. 2564–2571, Nov. 2010.

[38] N. Kuo, S. Gong, and G. Piazza, "Ultra high frequency phononic crystal in silicon carbide," in *Proc. 16th Int. Solid-State Sens., Actuators Microsyst. Conf.*, Jun. 2011, pp. 2486–2489.

[39] A. Ansari, H. Zhu, and M. Rais-Zadeh, "Gallium nitride high-order mode Lamb-wave resonators and delay-lines," in *Proc. Solid-State Sens. Actuators Microsyst. Workshop*, Jun. 2016, pp. 1–2.

[40] A. Siddiqui, R. H. Olsson, and M. Eichenfield, "Lamb wave focusing transducer for efficient coupling to wavelength-scale structures in thin piezoelectric films," *J. Microelectromech. Syst.*, vol. 27, no. 6, pp. 1054–1070, Dec. 2018.

[41] R. Feigelson, "Physics and chemistry of crystalline lithium niobate," *Science*, vol. 251, no. 5000, pp. 1510–1511, 1991.

[42] *IEEE Standard on Piezoelectricity*, IEEE Standard 176-1987, New York, NY, USA, 1987.

[43] R. Lu, M.-H. Li, Y. Yang, T. Manzaneque, and S. Gong, "Accurate extraction of large electromechanical coupling in piezoelectric MEMS resonators," *J. Microelectromech. Syst.*, vol. 28, no. 2, pp. 209–218, Apr. 2019.

[44] I. E. Kuznetsova, B. D. Zaitsev, S. G. Joshi, and I. A. Borodina, "Investigation of acoustic waves in thin plates of lithium niobate and lithium tantalate," *IEEE Trans. Ultrason., Ferroelectr., Freq. Control*, vol. 48, no. 1, pp. 322–328, Jan. 2001.

[45] C. S. Aartmann, S. Jen, M. A. Domalewski, and J. C. Andle, "Improved accuracy for determining SAW transducer capacitance and K2," in *Proc. IEEE Ultrason. Symp.*, Oct. 1987, pp. 161–168.

[46] R. Lu, T. Manzaneque, Y. Yang, and S. Gong, "Lithium niobate phononic crystals for tailoring performance of RF laterally vibrating devices," *IEEE Trans. Ultrason., Ferroelectr., Freq. Control*, vol. 65, no. 6, pp. 934–944, Jan. 2018.

[47] J. Zhou, T.-H. Chuang, T. Dinc, and H. Krishnaswamy, "Integrated wideband self-interference cancellation in the RF domain for FDD and full-duplex wireless," *IEEE J. Solid-State Circuits*, vol. 50, no. 12, pp. 3015–3031, Dec. 2015.

[48] Y. Yang, R. Lu, T. Manzaneque, and S. Gong, "Toward Ka band acoustics: Lithium Niobate asymmetrical mode piezoelectric MEMS resonators," in *Proc. IEEE Int. Freq. Control Symp. (IFCS)*, May 2018, pp. 1–5.

[49] I. E. Kuznetsova, B. D. Zaitsev, A. A. Teplykh, S. G. Joshi, and A. S. Kuznetsova, "The power flow angle of acoustic waves in thin piezoelectric plates," *IEEE Trans. Ultrason., Ferroelectr., Freq. Control*, vol. 55, no. 9, pp. 1984–1991, Sep. 2008.

[50] F. I. Fedorov, *Theory of Elastic Waves in Crystals*. New York, NY, USA: Springer, 2013. [Online]. Available: https://www.springer.com/us/book/9781475712773

[51] M. A. Biot, "General theorems on the equivalence of group velocity and energy transport," *Phys. Rev.*, vol. 105, no. 4, p. 1129, Feb. 1957.

[52] C. S. Lam and D. Gunes, "A low-loss SAW filter using two-finger per wavelength electrodes on the NSPUDT orientation of quartz," in *Proc. IEEE Ultrason. Symp.*, Oct./Nov. 1993, pp. 185–188.

[53] M. Goto, H. Yatsuda, and T. Chiba, "Power flow angles for slanted finger surface acoustic wave filters on langasite substrate," *Jpn. J. Appl. Phys.*, vol. 46, no. 7, p. 4744, 2007.

[54] F. Z. Bi and A. C. Pyman, "A fast algorithm of designing minimum phase transducer and its application to SPUDT filter design," in *Proc. IEEE Symp. Ultrason.*, Oct. 2003, pp. 522–525.

[55] G. Martin, F. Z. Bi, D. P. Chen, and C. S. Lam, "Synthesizing and optimizing SPUDT SAW filters," in *Proc. IEEE Symp. Ultrason.*, Oct. 1998, pp. 165–168.

[56] F. S. Hickernell, "Thin-films for SAW devices," *Int. J. High Speed Electron. Syst.*, vol. 10, no. 03, pp. 603–652, Sep. 2000.

[57] I. S. Didenko, F. S. Hickernell, and N. F. Naumenko, "The experimental and theoretical characterization of the SAW propagation properties for zinc oxide films on silicon carbide," *IEEE Trans. Ultrason., Ferroelectr., Freq. Control*, vol. 47, no. 1, pp. 179–187, Jan. 2000.

[58] S. Jyomura, K. Nagatsuma, and H. Takeuchi, "SAW propagation loss mechanism in piezoelectric ceramics," *J. Appl. Phys.*, vol. 52, no. 7, pp. 4472–4478, 1981.

[59] S. Gong and G. Piazza, "Monolithic multi-frequency wideband RF filters using two-port laterally vibrating lithium niobate MEMS resonators," *J. Microelectromech. Syst.*, vol. 23, no. 5, pp. 1188–1197, Oct. 2014.

[60] R. Lu and S. Gong, "Study of thermal nonlinearity in lithium niobate-based MEMS resonators," in *Proc. 18th Int. Conf. Solid-State Sens., Actuators Microsyst.*, Jun. 2015, pp. 1993–1996.

[61] K. M. Lakin, "Electrode resistance effects in interdigital transducers," *IEEE Trans. Microw. Theory Techn.*, vol. MTT-22, no. 4, pp. 418–424, Apr. 1974.

**Ruochen Lu** (S'14) received the B.E. degree (Hons.) in microelectronics from Tsinghua University, Beijing, China, in 2014, and the M.S. degree in electrical engineering from the University of Illinois at Urbana–Champaign (UIUC), Urbana, IL, USA, in 2017, where he is currently pursuing the Ph.D. degree.

His research interests include radio frequency (RF) microsystems and their applications for timing and signal processing.

Mr. Lu was a recipient of the Best Student Paper Awards at the 2017 IEEE International Frequency Control Symposium and 2018 IEEE International Ultrasonics Symposium, the 2015 Lam Graduate Award from the College of Engineering, UIUC, the 2017 Nick Holonyak, Jr. Graduate Research Award, the 2018 Nick Holonyak, Jr. Fellowship, and the 2019 Raj Mittra Outstanding Research Award from the Department of Electrical and Computer Engineering, UIUC.

**Tomás Manzaneque** (M'14) received the Ph.D. degree in industrial engineering from the University of Castilla–La Mancha, Ciudad Real, Spain, in 2015, with a focus on applying piezoelectric MEMS resonators as sensors for measuring the density and viscosity of liquids.

In 2015, he joined the Micro and Nanotechnology Laboratory, University of Illinois at Urbana–Champaign (UIUC), Urbana, IL, USA, as a Post-Doctoral Researcher, where he focused on acoustic devices for low-power radio receivers in the Internet of Things applications. In 2018, he moved to the Delft University of Technology, Delft, The Netherlands, as a Post-Doctoral Researcher, where he is currently working on microfluidic MEMS for biological applications. He has authored or coauthored more than 20 journal papers covering the design, modeling, characterization, and integration of piezoelectric microdevices.

**Yansong Yang** (S'15) received the B.S. degree in electrical and electronic engineering from the Huazhong University of Science and Technology, Wuhan, China, in 2014, and the M.S. degree in electrical engineering from the University of Illinois at Urbana–Champaign (UIUC), Urbana, IL, USA, in 2017, where he is currently pursuing the Ph.D. degree in electrical engineering.

His research interests include the design and microfabrication techniques of MEMS resonators, filters, and switches for RF front-ends and wake-up systems.

Mr. Yang won Second Place in the Best Paper Competition at the 2018 International Microwave Symposium. He was a finalist for the Best Paper Award at the 2018 IEEE International Frequency Control Symposium, and received the 2019 P. D. Coleman Graduate Research Award from the Department of Electrical and Computer Engineering, UIUC.

**Ming-Huang Li** (S'11–M'15) received the B.S. degree in mechanical engineering (minor in electrical engineering) from National Chung Cheng University, Chiayi, Taiwan, in 2009, and the M.S. and Ph.D. degrees from the Institute of NanoEngineering and MicroSystems, National Tsing Hua University, Hsinchu, Taiwan, in 2011 and 2015, respectively.

From 2016 to 2017, he was a Post-Doctoral Researcher at the Department of Power Mechanical Engineering, National Tsing Hua University. In 2017, he joined the Micro and Nanotechnology Laboratory, University of Illinois at Urbana–Champaign (UIUC), Urbana, IL, USA, as a Post-Doctoral Researcher. His research interests include micromechanical resonator and oscillator design for wireless communication and signal processing, MEMS-application-specified integrated circuit (ASIC) integration technologies, and interface circuit design for MEMS-based microsystems.

Dr. Li was a recipient of the Outstanding Engineering Student Scholarship from the Chinese Institute of Engineers in 2009, the Best Student Paper Award at the 2011 Joint Conference of the IEEE International Frequency Control Symposium, the European Frequency and Time Forum (IFCS-EFTF 2011), and the CTCI Foundation Science and Technology Research Scholarship in 2014.

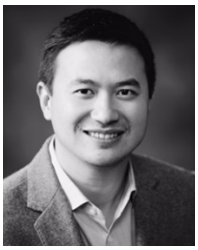

**Songbin Gong** (S'06–A'09–M'12–SM'17) received the Ph.D. degree in electrical engineering from the University of Virginia, Charlottesville, VA, USA, in 2010.

He is currently an Assistant Professor and the Intel Alumni Fellow with the Department of Electrical and Computer Engineering, Micro and Nanotechnology Laboratory, University of Illinois at Urbana–Champaign (UIUC), Urbana, IL, USA. His research primarily focuses on the design and implementation of radio frequency (RF) microsystems, components, and subsystems for reconfigurable RF front ends. In addition, his research explores hybrid microsystems based on the integration of MEMS devices with photonics or circuits for signal processing and sensing.

Dr. Gong was a Technical Committee Member of MTT-21 RF-MEMS of the IEEE Microwave Theory and Techniques Society, International Frequency Control Symposium, and International Electron Devices Meeting. He was a recipient of the 2014 Defense Advanced Research Projects Agency Young Faculty Award, the 2017 NASA Early Career Faculty Award, and the 2019 UIUC College of Engineer Dean's Award for Excellence in Research. Along with his students and postdocs, he received the Best Paper Awards from the 2017 and 2019 IEEE International Frequency Control Symposium, the 2018 International Ultrasonics Symposium, and Second Place in Best Paper Competition at the 2018 IEEE International Microwave Symposium. He has been a Guest Editor for the Special Issue on RF-MEMS in the *Journal of Micromechanics and Microengineering*.